PRAMANA
— journal of
physics

Vol. 57, Nos 2 & 3
Aug. & Sept. 2001
pp. 493–504

Proton scattering from unstable nuclei

Y BLUMENFELD[1], E KHAN[1], F MARÉCHAL[2*] and T SUOMIJÄRVI[1]
[1]Institut de Physique Nucléaire, IN_2P_3-CNRS, 91406 Orsay, France
[2]Department of Physics, Florida State University, Tallahassee Fl 32306, USA
[*]Present address: IRES, Strasbourg, France

Abstract. Recent improvements in the intensities and optical qualities of radioactive beams have made possible the study of elastic and inelastic proton scattering on unstable nuclei. The design and performances of an innovative silicon strip detector array devoted to such experiments are described. The quality of the data obtained are illustrated with recent results obtained at the GANIL facility for unstable oxygen, sulfur and argon isotopes. Methods to analyse the data using phenomenological and microscopic optical model potentials are discussed.

Keywords. Proton scattering; ^{34}Ar; ^{20}O; ^{30}S.

PACS No. 25.40.-h

1. Introduction

The detailed study of the properties of unstable nuclei has been at the forefront of nuclear physics research during recent years. The ultimate goal of such studies is to develop models and interaction potentials that can be applied to nuclei far from stability. Along the way, novel manifestations of nuclear structure should be uncovered, among which nuclear halos and skins, new regions of deformation, the disappearance of shell closures or the appearance of new magic numbers may be cited. With the continuous improvement of intensities and optical qualities of secondary radioactive beams, it has become possible to study nuclei far from stability through nuclear reactions such as Coulomb excitation [1] and more recently elastic and inelastic scattering [2], transfer [3] and knock-out [4] reactions.

In this talk we will focus on elastic and inelastic proton scattering from unstable nuclei. Elastic proton scattering yields information on the nuclear matter distributions and the effective nucleon–nucleon potentials. Inelastic scattering towards low lying collective states gives access to transition probabilities and nuclear deformations, and is a well suited tool to scan new regions of deformation. Comparison of inelastic transition probabilities measured through Coulomb and hadronic excitation should give access to the isoscalar or isovector nature of the states through the ratio of multipole transition matrix elements M_n/M_p. It is the hope that these measurements should be sensitive to novel types of nuclear structure such as neutron halos or skins.

Proton scattering experiments on unstable nuclei are performed in inverse kinematics, where the radioactive beam strikes a target containing the protons. The kinematics of the

reaction are reconstructed from the measurement of the energy and angle of the recoiling protons. The IPN-Orsay, CEA-Bruyères le Châtel and CEA-Saclay have designed and built a novel silicon strip array named 'MUST' [5], specifically tailored to such experiments. The characteristics of the array will be described and its performances illustrated with results from the $^{34}\mathrm{Ar}(p,p')$ reaction performed at GANIL. Methods to analyse such data using phenomenological and fully microscopic optical potentials will be presented and discussed. Examples of results obtained for oxygen, sulfur and argon isotopes will be shown.

2. Experimental method illustrated by the $^{34}\mathrm{Ar}(p,p')$ reaction

The $^{34}\mathrm{Ar}(p,p')$ reaction is chosen here as an example. The concepts underlying all proton scattering experiments with radioactive beams performed at GANIL and the NSCL/MSU are similar.

2.1 *Radioactive beam production*

In order to perform proton scattering experiments on unstable nuclei, the radioactive beam must be produced which impinges on a target containing the protons. For the production of ^{34}Ar a 95 MeV/A ^{36}Ar beam bombarded a 492mg/cm^2 ^{12}C target. The fragments were analysed using the alpha spectrometer, and the resulting beam was purified by inserting a 100 mg/cm^2 plastic degrader at the dispersive image point of this spectrometer. A resulting intensity of 130000 pps of ^{34}Ar at 47 MeV/A was obtained. The beam purity was 94%, the main contaminant being ^{33}Cl. However, the incoming nuclei were identified event by event as will be shown below. The radioactive beam was transported to the target chamber with a momentum acceptance of 0.6%. Different rigidity settings allowed us to produce in the same experiment a radioactive ^{30}S beam with $1.5 \cdot 10^4$ pps and a stable ^{32}S beam with $2.3 \cdot 10^5$ pps for which proton scattering was also measured.

2.2 *Experimental methods*

For proton scattering in inverse kinematics, the most efficient method to determine the excitation energy and scattering angle is to measure the energy and angle of the recoiling protons. Figure 1 shows the calculated kinematic plot for elastic and inelastic scattering to the 2_1^+ state at $E^* = 2.09$ MeV and the 3_1^- state at $E^* = 4.51$ MeV for the ^{34}Ar $+p$ reaction at 47 MeV/A. This figure demonstrates the necessity of measuring the recoiling protons between approximately 60° and 90° in the laboratory frame with an angular resolution of approximately 0.5° and an energy resolution around 100 keV.

The MUST detector [5], built in collaboration between the CEA Bruyères le Châtel, the IPN-Orsay and the SPhN CEA-Saclay has been designed to fulfill the requirements of such experiments. It consists of 8 large area Si-strip, Si(Li), CsI telescopes with associated electronics and data acquisition system. The first stage of the telescopes consists in a 300 μm thick 60 $\times$ 60 mm^2 Si-strip detector built by CANBERRA semiconductor with a strip pitch of 1 mm in both the horizontal and vertical directions. Each strip detector is backed by a lithium drifted silicon diode (Si(Li)) of approximately 3 mm compensated thickness and a 15 mm thick CsI crystal. Two columns of four telescopes each are mounted side by side

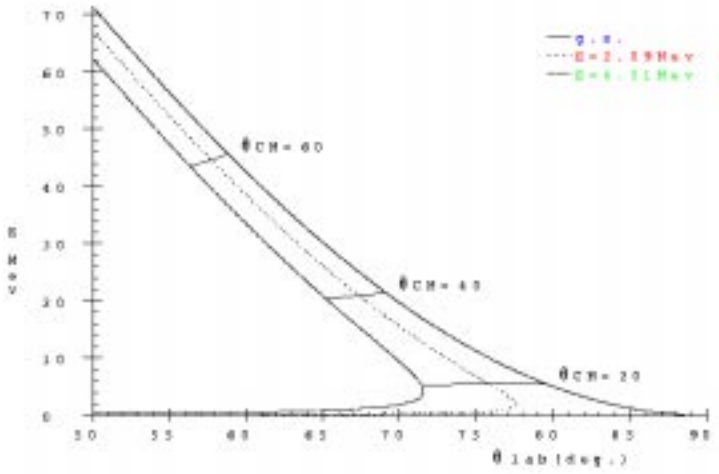

Figure 1. Laboratory energy vs angle of recoiling protons for ^{34}Ar(p, p') at 47 MeV/A. Solid line is for elastic scattering, dotted line for inelastic scattering towards the 2_1^+ state at 2.09 MeV, and dashed line for inelastic scattering towards the 3_1^- state at 4.51 MeV.

in the SPEG reaction chamber for the elastic and inelastic scattering experiments. Particles stopping in the first stage (protons of less than 6 MeV) are identified by energy and time of flight measurements, while higher energy particles traversing the strip detector are identified with the standard $\Delta E - E$ technique.

Because of the large emittance of the secondary beams, it is necessary to perform event by event ray tracing of the incoming nuclei. This was done with two low pressure multiwire proportional counters (CATS) [6] located 30 cm and 150 cm upstream from the target. These detectors yield a position resolution of approximately 0.3 mm in X and Y and also furnish a start signal for time of flight measurements with a resolution of 400 ps. These counters function reliably for counting rates up to $5 \cdot 10^5$ pps.

In order to select the reaction channel of interest and thus strongly reduce the background in the particle telescopes, the scattered nuclei were detected and identified in the focal plane of the SPEG spectrometer [7], through an energy loss measurement in a Bragg chamber and a time of flight measurement between a fast plastic scintillator and one of the tracking detectors.

2.3 *Results*

The left hand side of figure 2 displays the data for ^{34}Ar scattering in an energy vs. angle scatterplot for recoiling protons in coincidence with ^{34}Ar ejectiles detected in SPEG. The scattering angle has been corrected for the incident beam angle as well as for the impact position on the target. Kinematic lines corresponding to elastic scattering and inelastic scattering to the 2_1^+ state located at 2.1 MeV and 3_1^- state located at 4.5 MeV are clearly observed. The excitation energy and center of mass scattering angle are deduced from

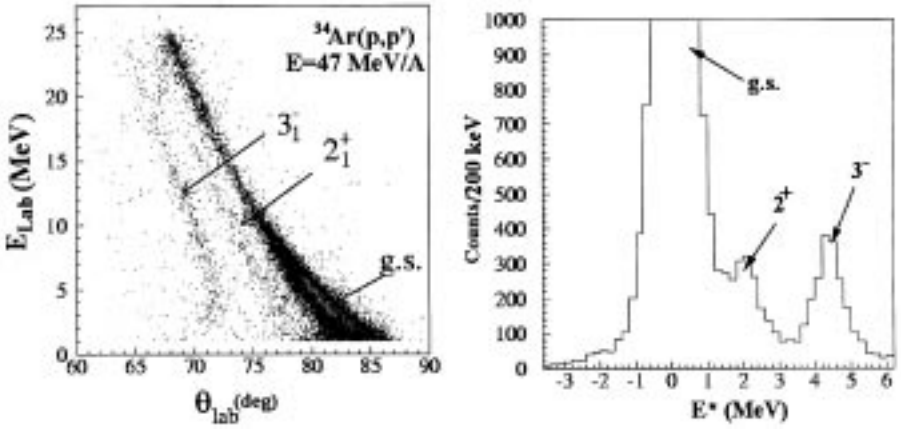

Figure 2. Left: Scatterplot of laboratory energy vs angle of recoiling protons for $^{34}\mathrm{Ar}(p,p')$ at 47 MeV/A. Right: Excitation energy spectrum deduced from left hand side plot.

the data through relativistic kinematics. The right hand side of figure 2 shows the resulting excitation energy spectrum where the three final states are clearly distinguished. The excitation energy resolution is approximately 700 keV, which is much worse than what is obtained in direct kinematics (p,p') scattering, thus exhibiting the main weakness of the method. Coincidences with a large solid angle Ge array would make possible such spectroscopy with much better energy resolution. Experiments combining MUST with the new germanium array EXOGAM currently under construction at GANIL are planned for the near future.

The angular distributions for the elastic and inelastic scattering are displayed on figure 3, which show the typical quality of the data that can be obtained. Up to now, with radioactive beams, the angular range measured is restricted to forward angles in the center of mass frame. An extension of the angular range accessible would be particularly interesting for elastic scattering, and will become possible with an increase of secondary beam intensities.

3. Methods of analysis

The Coulomb force is known exactly, so analyses of Coulomb excitation experiments are model independent [1]. On the other hand, extracting nuclear properties from proton scattering relies on interaction models, the parameters of which must be adjusted to reproduce experimental results. This consists in obtaining proton-nucleus optical potentials which can be used in DWBA or coupled channel calculations. Two methods are generally employed to carry out such analyses. The simplest approach is to use phenomenological optical potentials and standard collective form factors. In microscopic approaches, nuclear densities predicted by a nuclear structure model are folded with an effective nucleon–nucleon interaction to produce the optical potential. Details on the procedures used to analyse our data are given below.

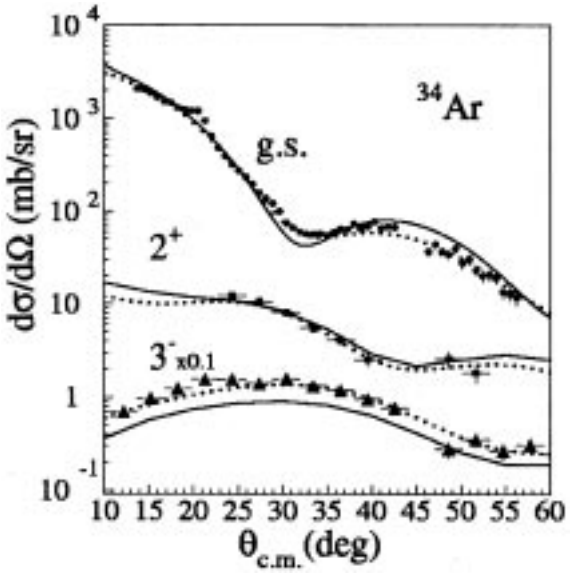

Figure 3. 47 MeV/A ^{34}Ar elastic and inelastic angular distributions for the 2_1^+ and the 3_1^- states. The dotted lines correspond to CCBA calculations using the Becchetti–Greenlees potential and the solid lines correspond to DWBA calculations using the JLM interaction folded with ground state and transition densities obtained with HF+BCS and QRPA models.

3.1 *Phenomenological analysis*

The aim is to extract deformation parameters for the low lying collective states through an analysis using DWBA calculations performed with the code ECIS [8] with phenomenological optical potentials and standard collective form factors. Compilations of many studies on stable nuclei have yielded optical model parametrizations such as that by Bechetti and Greenlees [9], which give good predictions for scattering cross sections. It must be checked that the optical potential used yields a good reproduction of the measured elastic scattering cross section for the unstable nucleus under study. The deformation parameters β_l of the excited states are then obtained by normalizing the calculated inelastic cross section to the data.

The combined measurements of inelastic hadron scattering and electromagnetic excitation (such as Coulomb excitation) of the same nuclei are interesting because they can provide a way to disentangle proton and neutron contributions to the studied transition. In the case of inelastic proton scattering at a few tens of MeV incident energy, the neutron interaction strength is three times larger than the proton one [10]. Therefore, proton scattering probes mainly the distribution of neutrons in the nucleus. In contrast, Coulomb excitation measures the electromagnetic transition strength $B(EL)$ which is the square of the proton multipole transition matrix element M_p in the case of an initial state with $J^\pi = 0^+$. Thus measurements of the deformation parameters with two different probes allows us to determine the ratio between the neutron and proton multipole transition ma-

trix elements M_n/M_p. In the phenomenological approach, this ratio is calculated using the formula derived in [11]:

$$\frac{M_n}{M_p} = \frac{b_p}{b_n}\left[\frac{\delta}{\delta_{\rm em}}\left(1+\frac{b_n}{b_p}\frac{N}{Z}\right)-1\right], \tag{1}$$

where b_p and b_n are the interaction strengths of incident protons with target protons and neutrons respectively, δ is the deformation length from (p,p') scattering and $\delta_{\rm em}$ is the electromagnetic deformation length ($\delta = \beta_l r_0\ A^{1/3}$). In the analysis of our data, an r_0 value of 1.17 fm which corresponds to the radius parameter of the Becchetti–Greenlees potential was used for (p,p') scattering, while $r_0 = 1.20$ fm was taken for electromagnetic excitation. The b_p and b_n values were taken as 0.3 and 0.7, respectively.

It must be cautioned that such a phenomenological approach may encounter difficulties far from stability due to the assumption of similar interaction potentials for neutrons and protons. Moreover, the extracted parameters are not directly related to the nuclear densities. Therefore, in order to obtain more detailed information, microscopic approaches are called for.

3.2 *Microscopic analysis*

A microscopic analysis is based on matter and transition densities calculated using a microscopic nuclear model. These densities are then folded with an effective complex nucleon–nucleon potential in order to obtain the proton–nucleus optical and transition potentials which can be used in DWBA calculations.

In the present work, we employed self-consistent microscopic models with Skyrme effective interactions, described in [12]. Neutron and proton matter densities are calculated in the Hartree–Fock+BCS model and the microscopic transition densities are obtained within the framework of the QRPA formalism. The only inputs to the calculations are the Skyrme interaction and the value of the constant pairing gap, Δ. In the calculations shown below, the SGII [13] parameterization is used, which has been shown to provide a somewhat better reproduction of the energies and transition strengths as compared to the SIII and SLy4 interactions [14]. The pairing effect, expected to be important in open-shell nuclei, is taken into account using the prescription $\Delta = 12A^{-1/2}$ MeV for the pairing gap. In order to calculate angular distributions complex optical and transition potentials were obtained by injecting the calculated ground state and transition densities into the Jeukenne, Lejeune and Mahaux (JLM) density dependent optical potential [15], which was derived from Brückner–Hartree–Fock nuclear matter calculations. Cross sections were then calculated in a DWBA approach with the TAMURA code [16].

Such an analysis provides a test of the densities and transition densities predicted by the nuclear model used. Ultimately it should provide a handle on the validity of effective interactions in nuclei far from stability, and consequently on the isospin dependence of these potentials. Moreover, an experimental value for the M_n/M_p ratio of excited states can be inferred, which does not suffer from the uncertainties of the phenomenological approach. This is done by assuming the validity of the shapes of the calculated transition densities, but allowing free normalizations. The comparison between the experimental value of $B(EL)$ measured with an electromagnetic probe, and the calculated value, fixes the proton transition density by setting the appropriate normalization. A renormalization

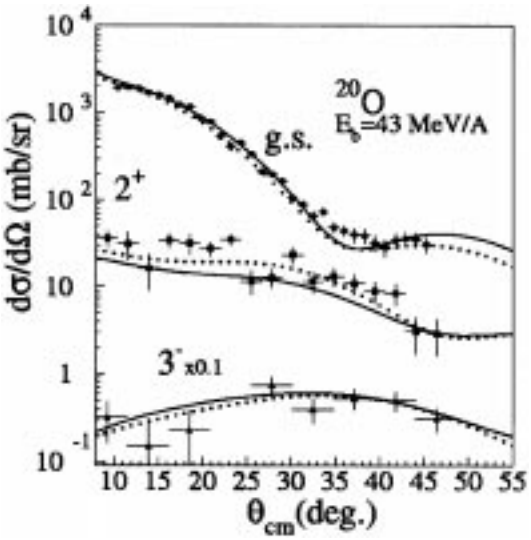

Figure 4. 43 MeV/A $(p, p')^{20}$O elastic and inelastic angular distributions for the 2_1^+ and 3_1^- states. The dotted lines correspond to CCBA calculations using the Bechetti–Greenlees optical potential and the solid lines correspond to DWBA calculations using the JLM interaction folded with ground state and transition densities obtained with HF + BCS and QRPA models.

of the calculated density is only necessary when the $B(EL)$ is not well reproduced by the theory. Once the M_p value is fixed, the M_n value is deduced by normalizing the neutron transition density in order to fit the measured (p, p') angular distribution.

In the remainder of the talk, the calculations described above will be confronted with our experimental results in the case of oxygen, sulfur and argon isotopes.

4. Results and discussion

4.1 ^{20}O

A secondary ^{20}O beam at 43 MeV/A was produced at GANIL using a primary ^{40}Ar beam at 77 MeV/A and scattering from a CH_2 target was measured using the MUST array. The scattering of a secondary ^{18}O beam at the same E/A was also measured for comparison [17]. For the ^{20}O case, the elastic and inelastic angular distributions for the 2_1^+ and 3_1^- states known to be located at 1.67 and 5.61 MeV respectively, are displayed on figure 4. The dotted lines are CCBA calculations using the Bechetti–Greenlees phenomenological optical potential. A very good reproduction of the elastic distribution is obtained. Normalization of the inelastic scattering calculations to the data yield deformation parameters β_2 = 0.55 ± 0.06 and β_3 = 0.35 ± 0.05.

Figure 5 displays the ground state and transition densities calculated in the framework of the HF + BCS and QRPA theories. The presence of a neutron skin is clearly visible. The DWBA cross sections using these densities and the JLM density dependant optical potential are shown as solid lines on figure 4. A small renormalization of the imaginary

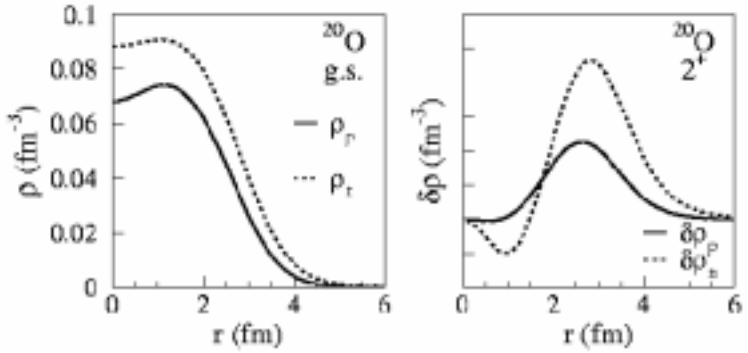

Figure 5. Left: Neutron and proton ground state density distributions for ^{20}O calculated with the HF + BCS model and the SGII Skyrme interaction. Right: Neutron and proton transition density distributions for the 2_1^+ state of ^{20}O calculated with the QRPA model and the SGII Skyrme interaction.

part of the potential ($\lambda_w = 0.8$) was applied in order to best reproduce the elastic angular distribution. Good agreement with the data is observed, which confirms the validity of the calculated ground state and transition densities. Using the procedure described in §3.2, a value of the ratio $M_n/M_p = 3.25 \pm 0.8$ is obtained for the 2_1^+ state. This value, in agreement with the prediction of the QRPA calculation [12], is much larger than $N/Z = 1.5$, demonstrating the strong neutron contribution to the excitation due to the presence of a neutron skin. A similar analysis in the case of the 2_1^+ state of ^{18}O yields $M_n/M_p = 1.10 \pm 0.24$, showing a very rapid structural change when adding 2 neutrons to go from ^{18}O to ^{20}O.

4.2 ^{30}*S and the sulfur isotopic chain*

Angular distributions for elastic and inelastic scattering to the 2_1^+ state in the neutron-deficient ^{30}S nucleus are displayed in figure 6. The dotted lines correspond to CCBA calculations using the Bechetti–Greenlees phenomenological potential. The agreement is very good, as was the case for the neutron-rich sulfur isotopes ^{38}S and ^{40}S [2]. Normalization of the inelastic calculation to the data yields a deformation parameter $\beta_2 = 0.32 \pm 0.03$, very similar to that of the $N = Z$ nucleus ^{32}S which has $\beta_2 = 0.30 \pm 0.02$. The solid lines correspond to the microscopic calculations performed taking $\lambda_w = 0.8$, and also reproduce the data well, apart from a small overestimation of the elastic scattering cross section at large angles. The comparison with electromagnetic measurements leads to $(M_n/M_p)/(N/Z) = 0.88 \pm 0.21$, compatible with 1. An inspection of the calculated densities does not show any evidence for a proton skin, contrarily to ^{38}S and ^{40}S for which a neutron skin is predicted.

It is interesting to follow the evolution of the ratio $(M_n/M_p)/(N/Z)$ as a function of neutron number, displayed in figure 7. For the n-rich isotopes ^{38,40}S, the electromagnetic measurements are taken from [18,19] and the proton scattering data from [2]. A good agreement between the experimental results and the QRPA predictions is observed. The most notable feature is the drop in $(M_n/M_p)/(N/Z)$ predicted for $N = 20$ and $N = 28$

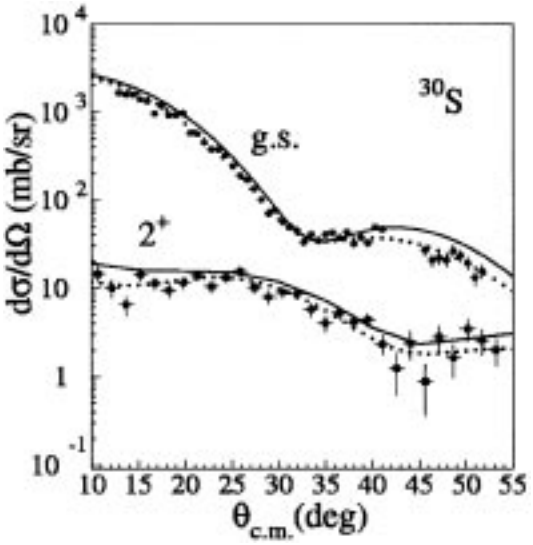

Figure 6. 53 MeV/A ^{30}S elastic and inelastic angular distributions for the 2_1^+ state. The dotted lines correspond to CCBA calculations using the Becchetti–Greenlees potential and the solid lines correspond to DWBA calculations using the JLM interaction folded with ground state and transition densities obtained with HF+BCS and QRPA models.

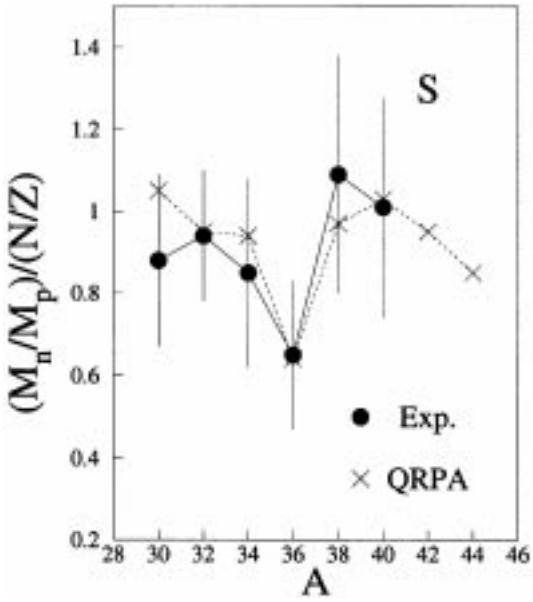

Figure 7. Values of the ratio $(M_n/M_p)/(N/Z)$ for the sulfur isotopic chain. Dots are experimental values extracted from the microscopic analysis (see text) and crosses are theoretical predictions from the QRPA calculations. Lines are eye-guides.

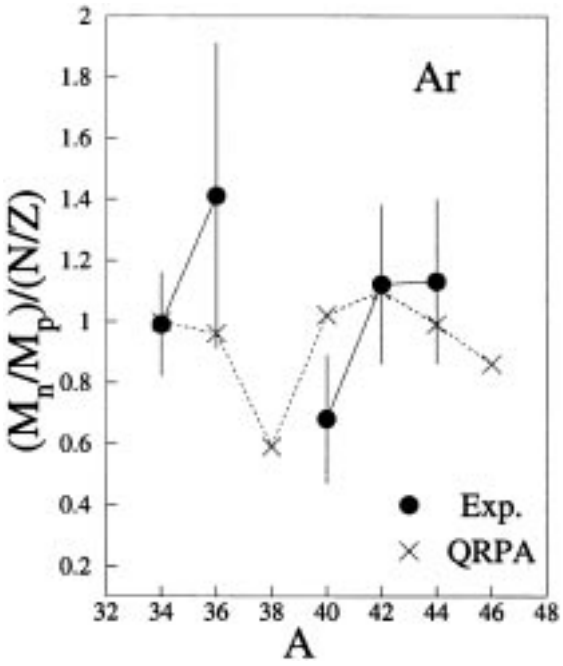

Figure 8. Values of the ratio $(M_n/M_p)/(N/Z)$ for the argon isotopic chain. Dots are experimental values extracted from the microscopic analysis (see text) and crosses are theoretical predictions from the QRPA calculations. Lines are eye-guides.

closed shells. This indicates that the quantity $(M_n/M_p)/(N/Z)$ is relevant for the study of the evolution of shell closures far from stability, and encourages us to pursue similar studies further from stability which should become possible with new generation radioactive beam facilities.

4.3 ^{34}*Ar and the argon isotopic chain*

Angular distributions for elastic and inelastic scattering to the 2_1^+ ans 3_1^- states in the neutron-deficient ^{34}Ar nucleus are displayed in figure 3. The dotted lines correspond to the phenomenological calculations, which yield deformation parameters $\beta_2 = 0.27 \pm 0.02$ and $\beta_3 = 0.39 \pm 0.03$. The microscopic calculations, performed with $\lambda_w = 0.8$, are represented by solid lines. The predictions deviate slightly from the data for $\Theta_{\rm cm} > 25^\circ$. If a value of $\lambda_w = 1$ is used, the largest angles are better reproduced at the expense of the minimum of the distribution. This might indicate a need for improvement of the imaginary part of the optical potential. The agreement between calculations and experiment is good for the 2_1^+ state while the cross section for the 3_1^- level is slightly underestimated. As in the case if ^{30}S, the calculated matter densities do not show any indication of a proton skin. The Coulomb barrier contains the additional protons inside the nucleus.

Figure 8 shows the evolution of the ratio $(M_n/M_p)/(N/Z)$ as a function of neutron number for the 2_1^+ states of argon isotopes. The values for the neutron-rich isotopes are

inferred from the data of [20]. No clear trend emerges from the experimental data, while the theoretical predictions show once again a strong decrease of $(M_n/M_p)/(N/Z)$ for neutron magic numbers $N = 20$ and 28.

5. Conclusions

The measurement of the angle and energy of recoiling protons has proven to be a well suited method for the study of proton elastic and inelastic scattering of unstable nuclei in reverse kinematics. Both phenomenological and microscopic approaches to analyse the data have been perfected. The latter is particularly powerful, as it provides the opportunity to test densities and transition densities predicted by various nuclear models, and thus assess the validity in hitherto unexplored regions of the nuclear chart of these approaches and of the effective nucleon–nucleon interactions on which they are based.

The advent of a new generation of radioactive beam facilities will extend the range of nuclei accessible for proton scattering measurements to more neutron rich species such as ^{44}S and ^{46}Ar, yielding additional information on the strength of the $N = 28$ shell closure far from stability. The improvement in beam intensities should also give access to larger center of mass angles, where the angular distributions should be more sensitive to the presence of neutron skins or halos.

Acknowledgements

We wish to thank our colleagues from IPN-Orsay, Florida State University, NSCL/Michigan State University, PTN-Bruyeres le Chatel and SPhN-Saclay for their participation in this proton scattering collaboration and the permission to present some of our recent results prior to publication.

References

[1] T Glasmacher, *Ann. Rev. Nucl. Part. Sci.* **48**, 1 (1998)
[2] F Maréchal *et al*, *Phys. Rev.* **C60**, 034615 (1999)
[3] S Fortier *et al*, *Phys. Lett.* **B461**, 22 (1999)
[4] A Navin *et al*, *Phys. Rev. Lett.* **85**, 266 (2000)
[5] Y Blumenfeld *et al*, *Nucl. Instrum. Methods Phys. Res.* **A421**, 471 (1999)
[6] S Ottini-Hustache *et al*, *Nucl. Instrum. Methods Phys. Res.* **A431**, 476 (1999)
[7] L Bianchi *et al*, *Nucl. Instrum. Methods Phys. Res.* **A276**, 509 (1989)
[8] J Raynal, *Phys. Rev.* **C23**, 2571 (1981)
[9] F D Bechetti Jr and G W Greenlees, *Phys. Rev.* **182**, 1190 (1969)
[10] A M Bernstein, V R Brown, and V A Madsen, *Phys. Lett.* **B103**, 255 (1981)
[11] A M Bernstein, V R Brown and V A Madsen, *Comm. Nucl. Part. Phys.* **11**, 203 (1983)
[12] E Khan and Nguyen van Giai, *Phys. Lett.* **B472**, 253 (2000)
[13] Nguyen van Giai and H Sagawa, *Nucl. Phys.* **A371**, 1 (1981)
[14] E Khan, PhD thesis, Université d'Orsay, Internal report IPNO-T-00-01
[15] J P Jeukenne, A Lejeune and C Mahaux, *Phys. Rev.* **C16**, 80 (1977)
[16] T Tamura *et al*, *Comp. Phys. Comm.* **2**, 94 (1971)

[17] E Khan *et al*, *Phys. Lett.* **B490**, 45 (2000)
[18] H Scheit *et al*, *Phys. Rev. Lett.* **77**, 3967 (1996)
[19] T Glasmacher *et al*, *Phys. Lett.* **B395**, 163 (1997)
[20] H Scheit *et al*, *Phys. Rev.* **C63**, 014604 (2001)